

Toward Improving Actuation Transparency and Safety of a Hip Exoskeleton With a Novel Nonlinear Series Elastic Actuator

Yuepeng Qian¹, Graduate Student Member, IEEE, Shuaishuai Han², Member, IEEE, Yining Wang³, Haoyong Yu⁴, Senior Member, IEEE, and Chenglong Fu⁵, Member, IEEE

Abstract—Actuation transparency and safety are important requirements in the design and control of assistive exoskeletons for individuals who suffer lower limb deficits but still maintain a certain level of voluntary motor control. In recent years, series elastic actuator (SEA) has been regarded as a promising solution for transparent actuation and safe human–robot interaction, thus SEAs are widely developed and applied in assistive exoskeletons. However, existing SEAs designed for assistive exoskeletons still lack both actuation transparency and safety because of high stiffness of the elastic element and the high mechanical impedance of the actuators. To address this problem, a novel nonlinear SEA (nSEA) is presented in this article. The optimized nonlinear series elastic element coupled with a

quasi-direct drive motor creates the nSEA with low mechanical impedance, high backdrivability, and less acoustic noise. Besides, a new torque control, based on cascade PI control, is proposed for the nSEA to control the interaction torque with high accuracy and robustness. Finally, an experimental evaluation with human subjects is performed to validate the advantages of the nSEA-driven hip exoskeleton in the realization of actuation transparency and safety. The root-mean-square interaction torque in zero-impedance mode is as low as 0.051 N · m during walking conditions, leading to a negligible negative influence on the hip joint's range of motion, walking speed, and energy expenditure when wearing the hip exoskeleton.

Index Terms—Cascade PI control, nonlinear series elastic actuator (nSEA), transparent actuation, wearable hip exoskeleton.

Manuscript received 23 September 2021; revised 2 January 2022 and 31 May 2022; accepted 18 August 2022. Date of publication 2 September 2022; date of current version 16 February 2023. Recommended by Technical Editor A. N. Vargas and Senior Editor W. J. Chris Zhang. This work was supported in part by the National Natural Science Foundation of China under Grant U1913205, in part by the Agency for Science, Technology and Research, Singapore, under the National Robotics Program, with A*star SERC Grant 192 25 00054 and Grant 192 25 00045, in part by the Stable Support Plan Program of Shenzhen Natural Science Fund under Grant 20200925174640002, and in part by the Science, Technology and Innovation Commission of Shenzhen Municipality under Grant ZDSYS20200811143601004. (Corresponding author: Chenglong Fu.)

Yuepeng Qian is with the Department of Biomedical Engineering, National University of Singapore, Singapore 117583, and also with the Shenzhen Key Laboratory of Biomimetic Robotics and Intelligent Systems and the Guangdong Provincial Key Laboratory of Human-Augmentation and Rehabilitation Robotics in Universities, Department of Mechanical and Energy Engineering, Southern University of Science and Technology, Shenzhen 518055, China (e-mail: yuepeng.qian@u.nus.edu).

Shuaishuai Han and Haoyong Yu are with the Department of Biomedical Engineering, National University of Singapore, Singapore 117583 (e-mail: han.ss@nus.edu.sg; biehy@nus.edu.sg).

Yining Wang and Chenglong Fu are with the Shenzhen Key Laboratory of Biomimetic Robotics and Intelligent Systems and the Guangdong Provincial Key Laboratory of Human-Augmentation and Rehabilitation Robotics in Universities, Department of Mechanical and Energy Engineering, Southern University of Science and Technology, Shenzhen 518055, China (e-mail: 11930460@mail.sustech.edu.cn; fucl@sustech.edu.cn).

This work involved human subjects or animals in its research. Approval of all ethical and experimental procedures and protocols was granted by the Institutional Review Board at the National University of Singapore under IRB approval No. (LH-20-012).

Color versions of one or more figures in this article are available at <https://doi.org/10.1109/TMECH.2022.3201255>.

Digital Object Identifier 10.1109/TMECH.2022.3201255

I. INTRODUCTION

IN RECENT years, various assistive lower-limb exoskeletons [1], [2], [3], [4] have been developed for people with weak mobility, such as incomplete paraplegic patients or elderly people with age-related mobility decline. Unlike paraplegic patients who lose motor function completely, incomplete paraplegic patients or elderly people are still able to perform voluntary motions, although the motor control is not fully functional due to muscle weakness and paralysis. Moreover, the motor control function of incomplete paraplegic patients or elderly people is not as robust as that of able-bodied people, and thus, their body systems become vulnerable to disturbances, such as external forces [1]. Therefore, the design and control of assistive exoskeletons for incomplete paraplegic patients or elderly people are very challenging, in which actuation transparency and safety are primary requirements [1], [5].

An actuator system is called transparent when it is able to perfectly generate any actuation force as desired [1], [6]. In order to provide effective assistance, the exoskeleton is expected to generate assistive torque only when the human needs assistance and to exhibit minimal resistance when assistance is not required. Therefore, actuation transparency is one of the most important requirements in the design of exoskeletons. Currently, common ways to achieve transparent actuation of assistive exoskeletons are through dynamic model compensation control [7], interaction force feedback control [8], [9], or impedance control [10], [11], [12]. However, the performance of software-based

transparency is still limited by the high mechanical impedance of actuators because the mechanical impedance cannot be completely compensated by control algorithms [10], [11], and these methods may have robustness issues in the presence of model inaccuracy or human–robot system variations [2].

In recent years, series elastic actuators (SEAs) have been widely applied in assistive exoskeletons because of their unique advantages compared to rigid actuators, including accurate force control, lower mechanical impedance, shock tolerance, and safety for physical human–robot interaction (pHRI) [13]. The introduction of a physical elastic element between the rigid actuator and the external load not only improves compliance in pHRI but also partially masks friction and reflected inertia in motors and transmission mechanisms [14], [15]. In this context, SEAs have been regarded as a promising solution for transparent actuation and safe pHRI in a number of research articles.

Nonetheless, existing SEAs designed for assistive exoskeletons are still unable to well satisfy the requirements for transparent actuation and safety. SEAs typically use springs with fixed stiffness as the elastic element in the force transmission and the performance of SEAs largely depends on the spring constant [16]. In order to meet the requirements for force output and force bandwidth, most existing SEAs designed for assistive exoskeletons [2], [17], [18] used springs with high stiffness, leading to compromised performance of actuation transparency and safety. In order to overcome the limitations of existing SEAs, some novel SEA designs were proposed. In [1] and [2], mechanical clutches were integrated into SEAs to automatically disengage and engage the force transmission, which was successfully applied in hip exoskeletons to improve actuation transparency and mechanical safety. However, these SEAs have the risk of system instability in the process of disengagement and engagement, and the introduction of a mechanical clutch also makes these SEAs more complicated and heavy. In addition to the SEAs with mechanical clutch, nonlinear SEAs [15], [19], [20], [21], [22] also provide a promising solution to the aforementioned limitations. But the designs of existing nonlinear SEAs still have limitations and lack special considerations for actuation transparency. In [19], [20], [21], and [22], the nonlinear stiffness was generated with various mechanisms, such as cam mechanism and hypocycloid mechanism, leading to cumbersome design and complicated stiffness/torque calculation [23], [24]. The hysteresis in rubber springs also introduced instability in high-frequency conditions (>1.5 Hz) [21]. Recently, a nonlinear SEA using linear tension springs was developed for an elbow exoskeleton, but the nonlinear stiffness profile was not optimal for improving actuation transparency, which was a compromise between performance and controllability [15]. Moreover, a conventional combination of low-torque motor and high-ratio gear reducer was widely used in existing SEAs [2], [15], [18], [22]. Large friction and reflected inertia from the high-ratio gear reducer also degraded the backdrivability of these SEAs.

To better assist incomplete paraplegic patients or elderly people, a novel nonlinear SEA (nSEA) is developed in this study. With a reconfigurable rotary series elastic element (RSEE) using linear tension springs, different stiffness profiles from nonlinear

to linear can be generated by choosing the different configuration of the RSEE. According to our previous study [25], nonlinear stiffness could significantly reduce mechanical impedance and improve backdrivability; thus, the configuration with a highly nonlinear stiffness is adopted to make full use of the benefits of nonlinear stiffness to improve actuation transparency and safety. Furthermore, the transmission mechanism is also optimized for low mechanical impedance and a quasi-direct drive motor is selected to drive the nSEA, which minimizes reflected inertia and friction in the transmission mechanism compared to existing SEAs that adopt high-ratio gear reducer. To the best of our knowledge, we are the first to integrate these features on a SEA. The nonlinear series elastic element coupled with a quasi-direct drive motor creates an actuator with low mechanical impedance and high backdrivability, which is significant for the realization of actuation transparency and safety.

Apart from the actuator design, high accuracy of force control is also crucial for the realization of transparent actuation and safety. But it is challenging to achieve with the nonlinear SEAs, especially the nonlinear SEAs with low stiffness. Cascade PI control has been widely applied in the force control of SEAs [26], [27], [28] because of its high stability, good robustness, and simple tuning process. In [26], Vallery et al. analyzed the conditions to passively control a linear SEA with cascade PI controller, and then, the controller was successfully implemented on an SEA-driven lower-limb exoskeleton called LOPES. The work presented in [28] further derived the necessary and sufficient conditions for passively rendering zero impedance and virtual springs with this cascade-control architecture. However, cascade PI control is mainly applied to linear SEAs and existing theoretical results only provide guidance for the force controller design of linear SEAs. For nonlinear SEAs, it remains challenging to acquire satisfactory performance as the nonlinear stiffness is included in the closed-loop dynamics, and the nonlinearity will limit the stability region [29]. Therefore, in practical applications, one usually has to find a compromise between stability and accuracy [15].

In this article, a new torque control, based on cascade PI control, is proposed for accurate and robust torque control of the nSEA, which considers the nonlinear kinematics in the controller design. Unlike linear SEAs, the desired deflection of nonlinear SEAs is difficult to be yielded through inverse kinematics due to the complexity of nonlinear kinematics. Thus existing nonlinear SEAs [15], [21] feed the desired torque command directly to the controller. In order to further improve the torque control performance, we adopt Newton–Raphson method to calculate the desired deflection angle of the RSEE according to the desired torque and feed it to the cascade PI controller. With such a transition, the nonlinearity can be excluded from the closed-loop dynamics and the cascade PI controller can be still designed with principles of a linear system. Finally, a detailed experimental evaluation with human subjects is performed, demonstrating the advantages of the nSEA-driven hip exoskeleton and the proposed torque controller in guaranteeing actuation transparency and safety.

The rest of this article is organized as follows. Section II describes the hip exoskeleton design and system hardware. The

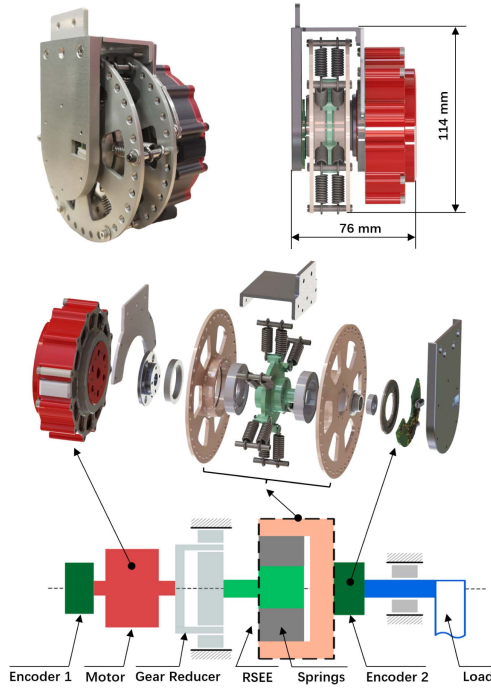


Fig. 1. Mechanical design of the proposed nSEA.

design and analysis of the new torque controller are presented in Section III. In Section IV, the experimental evaluation results of the nSEA-driven hip exoskeleton and its associated torque controller are presented. Finally, Section V discusses the experimental results and Section VI concludes this article.

II. HIP EXOSKELETON SYSTEM

A. Requirements for Hip Exoskeleton

The hip exoskeleton presented in this article was designed to provide assistance for hip flexion/extension (HFE) during walking, and the targeted users are incomplete paraplegic patients or elderly people with age-related mobility decline. During level-ground walking, the peak torque of the hip joint for HFE is approximately $0.8 \text{ N} \cdot \text{m/kg}$ with a walking speed of 1.1 m/s [30], and 99% of the power in kinematic signals is maintained below 6 Hz [31]. To meet the design criterion of providing 30% of the hip torque required during level-ground walking, the actuator needs to provide a peak torque of $16.8 \text{ N} \cdot \text{m}$ for a user with a body weight of 70 kg .

B. Nonlinear SEA Module

1) **Actuator Design:** As shown in Figs. 1 and 2, the nonlinear stiffness of the nSEA is generated by a novel and reconfigurable RSEE using linear tension springs, which is designed based on a coaxial rotation mechanism. In this design, two coaxial plates of the RSEE can rotate relatively and are coupled through the linear tension springs. The inner plate is actuated by the motor and the outer plate is linked to the external load. Then, the output torque of the nSEA is measured by indirectly measuring the deflection of the RSEE with two high-resolution absolute encoders.

TABLE I
NONLINEAR SEA CHARACTERISTICS

Parameter	Value	Unit
Peak output torque	19.8	N·m
Continuous output torque	6.6	N·m
Peak angular velocity	250	deg/s
Range of motion	± 135	deg
Max deflection of the RSEE	± 23.8	deg
Bandwidth with small output ($\pm 1.5 \text{ N} \cdot \text{m}$)	7.2	Hz
Bandwidth with large output ($7 \pm 1 \text{ N} \cdot \text{m}$)	24.2	Hz
Number of springs (n)	12	-
Spring stiffness (k)	24.5	kN/m
Range of equivalent stiffness (K_{eq})	[6.7, 112.9]	Nm/rad
Range of theoretical torque resolution (α)	[0.0004, 0.0072]	N·m
Size (length \times width \times thickness)	$114 \times 108 \times 76$	mm
Weight	0.85	kg

The stiffness of the RSEE is mainly determined by the spring stiffness, the number of springs, and the offset angle of springs. The parameters and number of tension springs are determined taking into account the maximum assistive torque required in our targeted application, as well as the restricted installation space in the RSEE. On the one hand, the tension springs with higher stiffness lead to higher stiffness and larger output torque of the RSEE at a large deflection angle. On the other hand, the stiffness of the RSEE around the initial position remains low due to the design characteristics of the RSEE, which can satisfy the need for establishing high transparency. Compared to the parameters and number of springs, the offset angle of springs can change the stiffness profile more significantly. With the increase of the offset angle, the nonlinearity becomes weaker and the stiffness and output torque at the same deflection angle are increased. In this study, to make full use of the benefits of nonlinear stiffness to improve actuation transparency and safety, a highly nonlinear stiffness profile ($\varphi = 0^\circ$) is adopted.

In order to further reduce the mechanical impedance of the nSEA, a quasi-direct drive motor (QDD-NU80-6, INNFOSS, Beijing, China) was selected to drive the nSEA. The ratio of planetary gear transmission is only 6:1, which enables low-impedance actuation with less acoustic noise [5], [32]. After the transmission, the nSEA is capable of providing a continuous torque of $6.6 \text{ N} \cdot \text{m}$ and a peak torque of $19.8 \text{ N} \cdot \text{m}$ with an angular velocity of up to $250^\circ/\text{s}$. All characteristics of the nSEA module are summarized in Table I, and it can be found that the properties of the nSEA module completely satisfy the requirements of our targeted application.

2) **Modeling and Experimental Validation:** According to the mechanical design of the reconfigurable RSEE, the kinematic model is established and all geometrical parameters illustrated in Fig. 2(b) are defined as follows:

- 1) φ denotes the offset angle at the initial position.
- 2) l_0 , Δl denote the spring rest length and the spring pre-tension length, respectively. Especially, Δl is set to be 0.5 mm , which is necessary to overcome the initial tension of the selected spring and avoid the completely relaxed situation of the RSEE when $\varphi = 0^\circ$.
- 3) r_1 , r_2 denote the radius of the hitching points of the inner and outer plate, respectively. Specifically, r_2 is

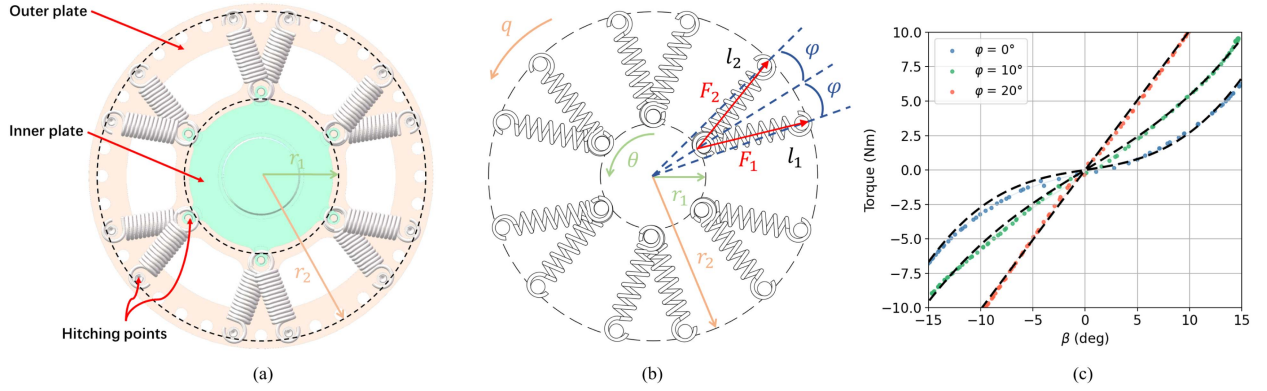


Fig. 2. Design and modeling of the reconfigured RSEE. (a) Front view of the reconfigured RSEE. (b) Schematic of the reconfigured RSEE. Depending on the offset angle of springs in the reconfigurable RSEE, different stiffness profiles from nonlinear to linear can be yielded. (c) Model validation results. The dots and black dashed lines represent the experimental results and the theoretical predictions, respectively.

determined according to the following equation:

$$r_2 = r_1 + l_0 + \Delta l. \quad (1)$$

- 4) θ, q denote the rotation angle of the inner and outer plate, respectively, and the deflection angle of the RSEE can be yielded according to the following equation:

$$\beta = \theta - q. \quad (2)$$

- 5) l_1 and l_2 denote the length of the two springs in each pair at any angle of deflection and can be calculated based on cosine law using the following equation:

$$\begin{cases} l_1 = \sqrt{r_1^2 + r_2^2 - 2r_1r_2 \cos(\beta + \varphi)} \\ l_2 = \sqrt{r_1^2 + r_2^2 - 2r_1r_2 \cos(\beta - \varphi)} \end{cases}. \quad (3)$$

- 6) F_i ($i = 1, 2$) represents the tension force of the two springs in each pair and can be calculated according to Hooke's law as follows:

$$F_i = k(l_i - l_0). \quad (4)$$

With the measurement of the deflection angle β , the output torque of the nSEA can be calculated by

$$\begin{aligned} \tau_e = f(\beta) = nkr_1r_2 & \left[\left(1 - \frac{l_0}{l_1}\right) \sin(\beta + \varphi) \right. \\ & \left. + \left(1 - \frac{l_0}{l_2}\right) \sin(\beta - \varphi) \right] \end{aligned} \quad (5)$$

where n denotes the number of spring pairs.

The equivalent rotational stiffness of the rotary nSEA is defined by

$$\delta\tau_e = K_{eq} \cdot \delta\beta. \quad (6)$$

That is

$$K_{eq} = \frac{\delta\tau_e}{\delta\beta} = \frac{\delta\tau_e}{\delta(\theta - q)}. \quad (7)$$

In order to validate the accuracy of the kinematic model, a validation experiment was performed to compare the experimental torque-deflection characteristics of the RSEE with the theoretical results of (5). During the experiment, a six-axis force/torque

sensor (Mini58, ATI Industrial Automation, Apex, USA) was connected to the output side of the RSEE to measure the actual output torque while the estimated output torque was calculated with the measured RSEE deflection angle. As shown in Fig. 2(c), compared to the theoretical predictions, the experimental results had a root-mean-square (rms) error of 0.28, 0.24, 0.22 N·m for the three configurations of the RSEE ($\varphi = 0^\circ, 10^\circ, 20^\circ$), which was less than 3.6%, 2.6%, 2.1% of the peak applied load. The close correlation between the experimental results and the theoretical predictions validated the high accuracy of the kinematic model. Moreover, simulation analysis was also performed based on the validated kinematic model, and simulation results show that the equivalent rotation stiffness of the nSEA can vary from 6.7 N·m/rad to 112.9 N·m/rad for the adopted configuration ($\varphi = 0^\circ$), depending on the deflection of the RSEE.

C. Hip Exoskeleton Design

As shown in Table I, the hip exoskeleton driven by the nSEA [see Fig. 3(a)] allows $\pm 135^\circ$ range of motion in the sagittal plane, which is sufficient for HFE. Additionally, in order not to restrict the motion of hip joint in the frontal plane, a passive hinge joint that allows $\pm 30^\circ$ range of motion is utilized to provide a degree of freedom for hip abduction/adduction (HAA). The exoskeleton is comfortably attached to the user through a commercial orthosis (including a waist band and a thigh cuff), which can be adjusted to accommodate different body sizes. The overall weight of the hip exoskeleton is around 2 kg where the main components of the hip exoskeleton are the nSEA module (0.85 kg each), the orthosis (0.58 kg for the waist brace and 0.36 kg for the thigh brace), other structural parts and sensors (0.2 kg). Currently, the hip exoskeleton is a unilateral device. Based on the modular design, it also can be extended to a bilateral device if necessary.

D. System Hardware Configuration

The hardware configuration of the hip exoskeleton system is shown in Fig. 3(c). The high-level control system was built based on a PC/104 CPU board (PCM-3365 N, Advantech, Singapore) to control the nSEA through a controller area network

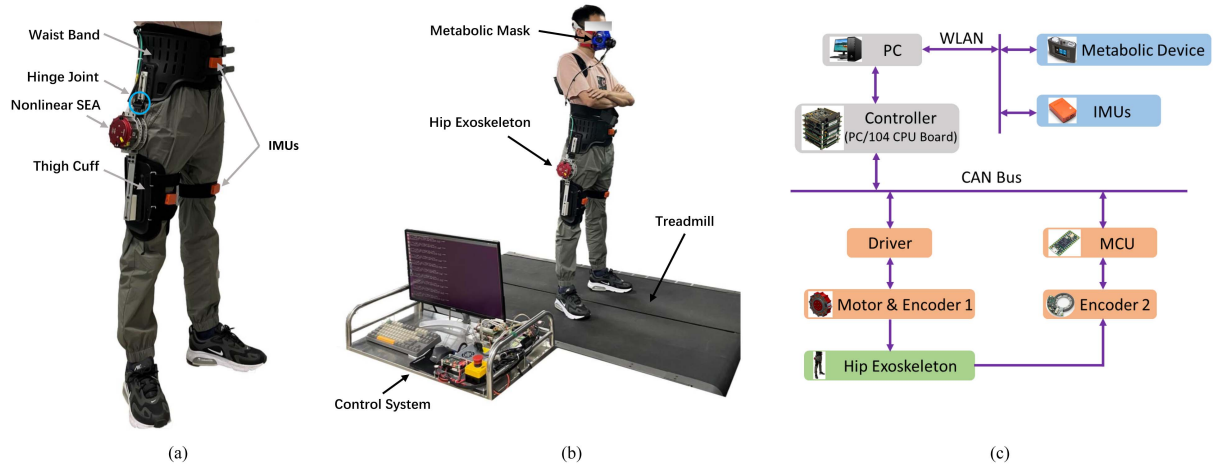


Fig. 3. Hip exoskeleton design and system hardware configuration. (a) Unilateral hip exoskeleton design, mainly consisting of an nSEA module, a hinge joint, IMUs, and the orthosis (including the waist band and the thigh cuff). (b) Experimental setup of the exoskeleton testing. (c) Hardware configuration of the system. The system is comprised of 1) a hip exoskeleton (green); 2) actuator system (orange), including motor, driver, encoders, and MCU for data reading; 3) a high-speed control system (gray); 4) sensors (blue) that measure metabolic cost and hip movement during walking.

(CAN) bus. The deflection of the RSEE is monitored by position feedback from the encoder 1 embedded in the quasi-direct drive motor and the encoder 2 (MB039, RLS, Komenda, Slovenia) placed beside the output side of the RSEE. Moreover, the hip joint movement and metabolic cost are measured by wireless inertial measurement units (MTw, Xsens, Enschede, Netherlands) and a portable metabolic analyzer (K5, Cosmed, Rome, Italy), respectively, in real time during the experiments.

III. TORQUE CONTROL

A. Modified Cascade PI Control

In order to design a torque controller for the nSEA, the dynamics from the motor side to the output torque should be established. For the convenience of explanation, mechanical drawbacks like friction and backlash are neglected here. According to the work in [33], the nonlinear force dynamics of the nSEA is formulated as

$$J\ddot{\theta} + \tau_e(\theta - q) = \tau_m \quad (8)$$

where J is the moment of inertia of the motor and other mechanical parts of the nSEA, and τ_m is the motor torque. Conventional cascade PI controller directly generates the control input from the feedback signal $\tau_e(\theta - q)$ and θ . This introduces the nonlinearity of $\tau_e(\theta - q)$ into the closed-loop dynamics and makes it difficult to analyze the closed-loop stability. To address this issue, we convert the torque control to an equivalent position control task.

As shown in Fig. 4, a desired deflection angle is online calculated according to the desired torque, and the cascade PI controller aims to track the desired deflection angle $\beta_d = (\theta - q)_d$. However, from the kinematics of (5), it is difficult to find an analytical solution of the deflection angle $\beta = \theta - q$ according to the torque τ_e through inverse kinematics. In this article, we utilize the Newton–Raphson method to obtain a numerical

solution, which can be formulated as

$$\beta_i = \beta_{i-1} - \frac{\tau_e(\beta_{i-1}) - \tau_e(\beta)}{\partial \tau_e(\beta_{i-1}) / \partial \beta_{i-1}} \quad (9)$$

where i denotes the i_{th} sampling point. Simulation and experimental results show satisfactory accuracy in acquiring the desired deflection angle according to the desired torque with the Newton–Raphson method. In addition, to further handle the effects of nonlinear stiffness and decrease the burden of the cascade PI controller, a feedforward term is added to the modified cascade PI control, which leads to the following control law:

$$\tau_m = u + \tau_d \quad (10)$$

where τ_d is the feedforward term and u is generated by the modified cascade PI control. The position-loop PI controller is

$$\begin{aligned} \dot{\theta}_d &= \left(k_{pp} + k_{pi} \frac{1}{s} \right) [(\theta - q)_d - (\theta - q)] \\ &= \left(k_{pp} + k_{pi} \frac{1}{s} \right) (\beta_d - \beta) \end{aligned} \quad (11)$$

and the velocity-loop PI controller is

$$u = \left(k_{vp} + k_{vi} \frac{1}{s} \right) (\dot{\theta}_d - \dot{\theta}) \quad (12)$$

where s denotes the Laplace operator. Therefore, the entire control law can be written as

$$\tau_m = \left(k_{vp} + k_{vi} \frac{1}{s} \right) \left[\left(k_{pp} + k_{pi} \frac{1}{s} \right) (\beta_d - \beta) - \dot{\theta} \right] + \tau_d. \quad (13)$$

From the Bode diagrams shown in Fig. 5, the closed-loop stability can be guaranteed and the disturbance over a wide range of frequencies can be eliminated.

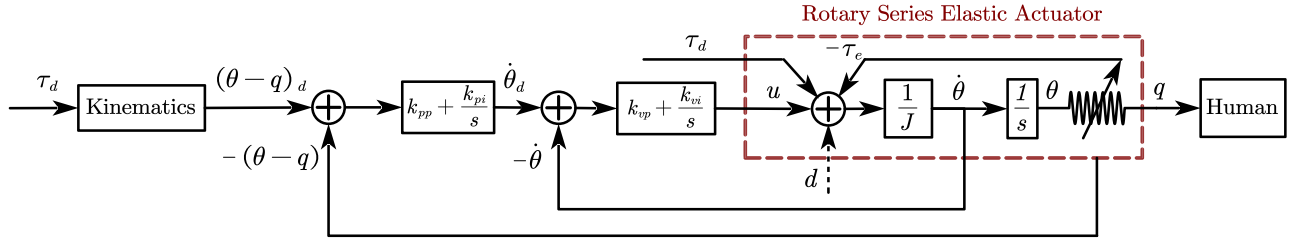


Fig. 4. Modified cascade PI control. With online kinematic computation, the torque control is converted into position control and the nonlinearity is excluded from the control loop.

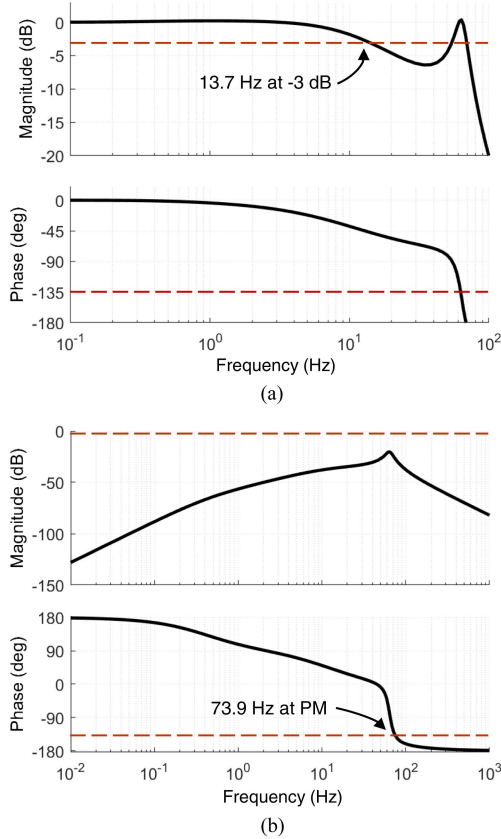


Fig. 5. (a) Bode diagram of the closed-loop dynamics. (b) Bode diagram of the sensitivity function.

B. Stability and Robustness Analysis

For the sake of explanation, the link-side angle is set to be zero ($q = 0$), which is reasonable as the link-side dynamics is usually lower than the SEA dynamics [34] and human limb will not aim to destabilize the system [28]. From Fig. 4 and (13), the closed-loop transfer function from the desired input to the actual output is

$$\frac{\beta(s)}{\beta_d(s)} = \frac{(k_{vp}s + k_{vi})(k_{pp}s + k_{pi})}{Js^4 + (s^2 + k_{pp}s + k_{pi})(k_{vp}s + k_{vi})}. \quad (14)$$

Clearly, with proper tuning of the PI control parameters, the eigenvalues of the closed-loop system can be assigned to the left half plane so that the entire system can be stabilized with specified convergence characteristics. The performance of

torque control can be regulated according to the application requirements.

As the velocity-loop dynamics possesses a much wider bandwidth than the torque-loop or position-loop, the cascade PI control is robust to external disturbance or internal uncertainties. In order to show the system robustness, the sensitivity function from the disturbance to the output is derived, and the disturbance is denoted as an equivalent input disturbance d in Fig. 4. For the ease of explanation, the desired torque is set to be zero here. The sensitivity function is

$$\frac{\beta(s)}{d(s)} = \frac{s^2}{Js^4 + (s^2 + k_{pp}s + k_{pi})(k_{vp}s + k_{vi})}. \quad (15)$$

From the sensitivity function, if the closed-loop dynamics in (14) is well tuned, the cascade PI controller can effectively eliminate the unknown disturbance from external or internal perturbations. In practical applications, one can design the performance of disturbance rejection by choosing proper parameters ($k_{pp}, k_{pi}, k_{vp}, k_{vi}$). For an intuitive illustration of the closed-loop stability and robustness, the Bode diagrams of the closed-loop transfer function and the sensitivity function are shown in Fig. 5.

IV. EXPERIMENTS AND RESULTS

Based on the hip exoskeleton design described in Section II and the proposed torque control method presented in Section III, the following performance characteristics were expected to be verified by experiments:

- 1) precisely generating the desired torque in the presence of human-exoskeleton system variations;
- 2) clearly demonstrating the advantages of high actuation transparency in human-exoskeleton interaction;
- 3) effectively guaranteeing the user's safety based on the high actuation transparency and good backdrivability of the proposed device.

All experimental protocols were approved by the Institutional Review Board at the National University of Singapore (NUS-IRB reference LH-20-012), and all participants provided consent before completing the experimental protocols.

A. Control Performance Validation

In this section, the effectiveness of the proposed controller was evaluated through tests with human subjects. To validate the advantages of the modified cascade PI controller, the control

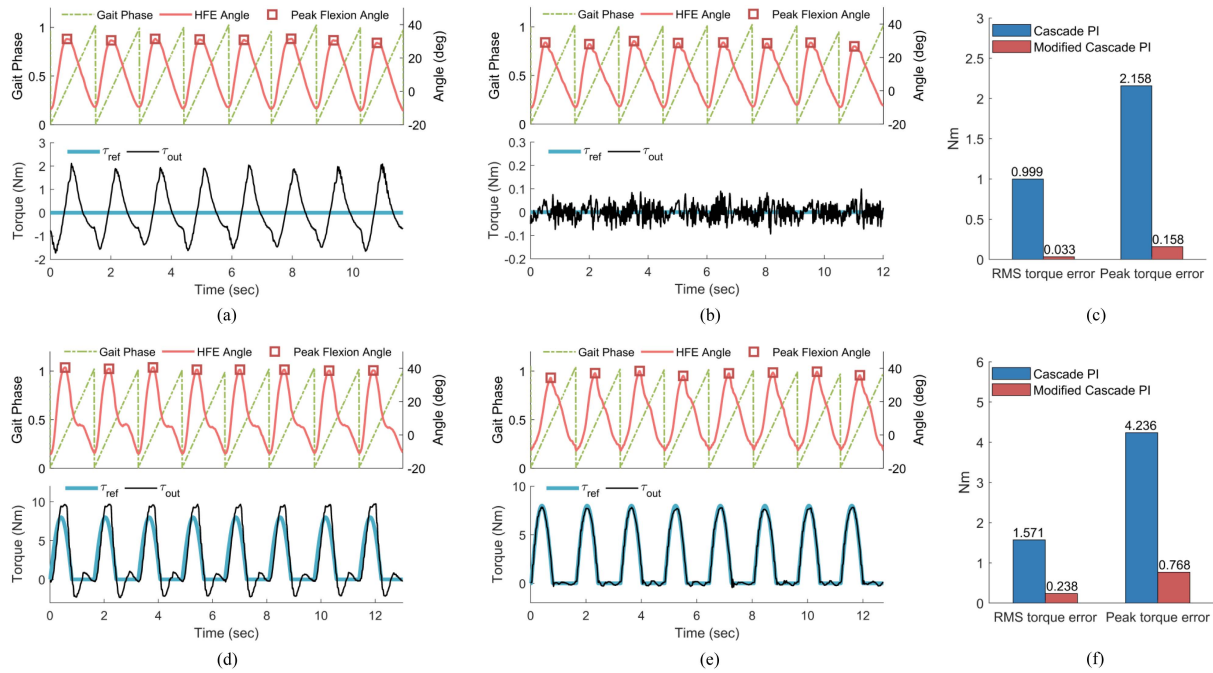


Fig. 6. Experimental results of torque control during continuous walking. (a) Zero-impedance control with the cascade PI controller. (b) Zero-impedance control with the modified cascade PI controller. (c) Comparison of the zero-impedance control performance. (d) Assistive control with the cascade PI controller. (e) Assistive control with the modified cascade PI controller. (f) Comparison of the assistive control performance.

TABLE II
CONTROLLER PARAMETERS

Symbol	Description	Value
k_{pp}	Proportion gain of the position loop	50
k_{pi}	Integration gain of the position loop	1200
k_{vp}	Proportion gain of the velocity loop	0.1
k_{vi}	Integration gain of the velocity loop	10

performance of the traditional cascade PI controller and the modified cascade PI controller are compared. To facilitate fair comparison, all experimental data were collected from the same subject (male; age, 24; weight, 65 kg; height, 170 cm) and the subject walked at the same speed of 0.8 m/s during the tests.

For the tuning of controller parameters, primary simulation was conducted in MATLAB/Simulink software and the parameters were determined by regulating the closed-loop transfer function (14). Then, the parameters yielded from the simulation were applied to the exoskeleton device. With minor manual tuning, satisfactory performance was achieved and the final controller parameters are summarized in Table II.

1) Transparency Test: In this test, the subject was asked to wear the hip exoskeleton and walk on the treadmill for 2 min with zero-impedance control of the cascade PI controller and the modified cascade PI controller, respectively.

As shown in Fig. 6(a), with the zero-impedance control of the cascade PI controller, the rms residual torque was $0.999 \text{ N} \cdot \text{m}$ while the peak residual torque was more than $2.1 \text{ N} \cdot \text{m}$. In contrast, as shown in Fig. 6(b), with the zero-impedance control of the modified cascade PI controller, the rms residual torque was only $0.033 \text{ N} \cdot \text{m}$ while the peak residual torque was $0.158 \text{ N} \cdot \text{m}$, which demonstrates the advantages of the proposed controller in

minimizing undesired resistance and ensuring the user's safety during walking.

2) Assistive Walking: In practical applications, the desired assistive torque should be determined by the exoskeleton's particular target. But evaluating the effects of the assistive strategy was beyond the goal of this study, and this article only focused on torque control of the nSEA during walking. Therefore, a curve torque signal was used as the desired trajectory of assistive torque for testing purposes. The nSEA output assistive torque during the early-swing phase (from toe-off to maximum hip flexion angle). As shown in Fig. 6(d) and (e) and compared in Fig. 6(f), with the control of the modified cascade PI controller, the rms error of the assistive torque was significantly reduced from $1.571 \text{ N} \cdot \text{m}$ to $0.238 \text{ N} \cdot \text{m}$, which validates the effectiveness of the proposed torque controller in the presence of fast human motions and human – exoskeleton system variations. Moreover, compared to zero-impedance mode, the peak hip flexion angle was significantly increased from $28.52 \pm 0.93 \text{ deg}$ to $36.71 \pm 1.38 \text{ deg}$ with the assistive torque from the exoskeleton, which illustrates the capability and potential of the exoskeleton in reducing joint movement deficits of paraplegic patients or elderly people.

B. Human–Exoskeleton Performance Characterization

This experiment was conducted to characterize the performance of the proposed device and validate the significance of high actuation transparency in human–exoskeleton interaction. Five healthy male subjects (age 24.2 ± 2.4 years; weight $64.4 \pm 8.9 \text{ kg}$; height $174 \pm 5 \text{ cm}$; and mean \pm SD) participated in this testing.

1) Experimental Design: The subjects walked on a treadmill with a walking speed of 0.8 m/s under four different conditions: 1) without exoskeleton, 2) with exoskeleton weight, 3) exoskeleton powered OFF, and 4) exoskeleton in zero-impedance mode. The without exoskeleton condition provides baseline information to compare and quantify the influences of the proposed device (such as the interaction impedance and the device weight) on the users in terms of hip movement and metabolic cost. Specifically, we have added the with exoskeleton weight condition where the subjects walked with an external load of the same weight as the exoskeleton but no interaction torque was exerted to the subjects. This condition can provide an additional baseline information (along with the without exoskeleton condition) to further distinguish the influence of the interaction impedance and the device weight on the users.

During all experimental conditions, the metabolic cost of the subjects was measured using a metabolic testing system and the modified Brockway equation [35]. Before the subjects began walking, their resting metabolic rate was measured for the last 2 min of a 5-min testing while they stood still without wearing the exoskeleton. Then, the metabolic rate of walking under the four experimental conditions was recorded for the last 2 min of each 6-min trail to calculate the walking energy expenditure while interaction torque and kinetic data were also recorded synchronously. The testing sequence of different experimental conditions is the same for each subject and a 5–8 min rest was taken between different tests according to the feedback of the subjects. After experimental data collection was completed, one-way analysis of variance (ANOVA) was used to compare changes in interaction torque, hip movement, and metabolic cost among the different experimental conditions, and a statically significant difference was defined as $p < 0.05$.

2) Results: After subtracting out the testing metabolic cost, the average net metabolic cost of walking were measured to be 1.95 ± 0.15 W/kg, 2.16 ± 0.20 W/kg, 2.15 ± 0.20 W/kg, and 2.24 ± 0.24 W/kg for the without exoskeleton, the with exoskeleton weight, the exoskeleton in zero-impedance mode, and the exoskeleton powered OFF condition, respectively. Compared to the without exoskeleton condition, it was observed that the with exoskeleton weight condition increased the net metabolic cost of walking. This result is unsurprising and the metabolic cost increase of walking is related to the exoskeleton weight added [36]. However, changes in the net metabolic cost of walking between the without exoskeleton condition and the with exoskeleton weight condition were not found to be significant ($p = 0.4404$), which benefits from the lightweight design of the exoskeleton device.

The metabolic cost compensation from the zero-impedance mode aligned well with the interaction torque compensation results [see Figs. 7(a) and 8]. With zero-impedance control of the proposed controller, the rms interaction torque between the human user and the exoskeleton was further reduced from $0.143 \text{ N} \cdot \text{m}$ to $0.051 \text{ N} \cdot \text{m}$. The small interaction torque in zero-impedance mode was negligible for the human users, resulting in almost equal walking energy expenditure under the with exoskeleton weight and the exoskeleton in zero-impedance

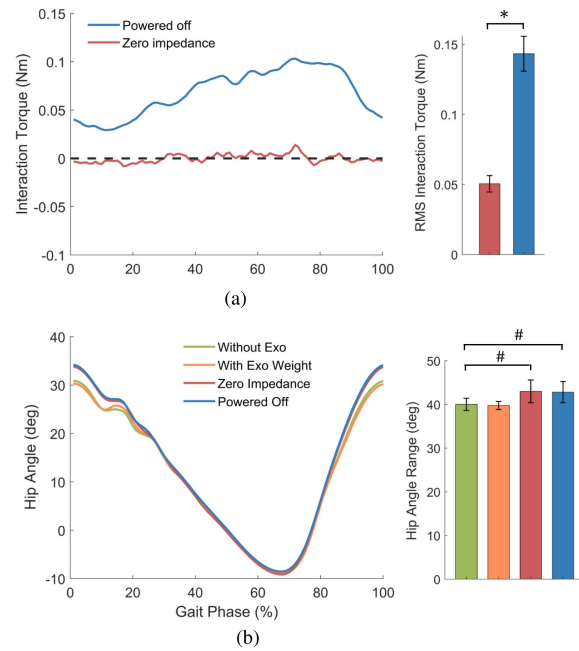


Fig. 7. Human-exoskeleton performance characterization results. (a) Interaction torque between human and the exoskeleton device under different actuator conditions. (b) Hip joint kinematics under different experimental conditions. Error bar in the graphs represents ± 1 SEM. * represents statically significant difference ($p < 0.05$) while # represents no statically significant difference.

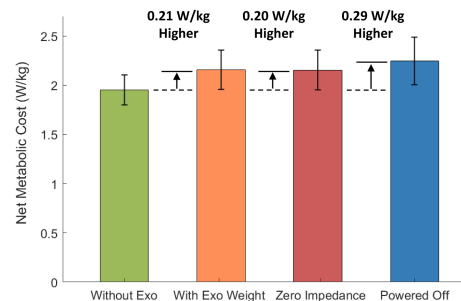


Fig. 8. Net metabolic costs under different experimental conditions (mean \pm SEM).

mode condition. Apart from the metabolic costs and the interaction torques, a more in-depth investigation was performed by observing the effect of the interaction torques on human gait biomechanics during walking, specifically on hip joint angle [see Fig. 7(b)]. The kinetic results demonstrated that the interaction torques did not impede the user's hip joint motion. No significant changes in the hip joint's range of motion with respect to the without exoskeleton condition were observed, for either the exoskeleton in zero-impedance mode condition ($p = 0.3438$) or the exoskeleton powered OFF condition ($p = 0.3463$). This is due to the high actuation transparency and good backdrivability of the exoskeleton, which illustrates the advantages of the design and control of the nSEA. These testing results, which are summarized in Table III, also demonstrate the significance of high actuation transparency in human-exoskeleton interaction.

TABLE III
HUMAN-EXOSKELETON PERFORMANCE CHARACTERIZATION RESULTS ACROSS DIFFERENT EXPERIMENTAL CONDITIONS AND SUBJECTS

Experimental Condition	Peak Flexion (deg)	Peak Extension (deg)	Range of Motion (deg)	RMS Interaction Torque (N·m)	Net Metabolic Cost (W/kg)
Without Exo	30.98 ± 1.86	-9.05 ± 0.68	40.03 ± 0.63	-	1.95 ± 0.15
With Exo Weight	30.70 ± 1.49	-9.07 ± 0.62	39.78 ± 0.94	-	2.16 ± 0.20
Zero Impedance	33.78 ± 2.31	-9.23 ± 0.88	43.00 ± 1.17	0.051 ± 0.006	2.15 ± 0.20
Powered OFF	34.20 ± 2.31	-8.66 ± 1.10	42.83 ± 1.10	0.143 ± 0.012	2.24 ± 0.24

All of the joint kinematic and kinetic results, the rms interaction torques and the net metabolic costs are presented with mean ± SEM across five subjects.

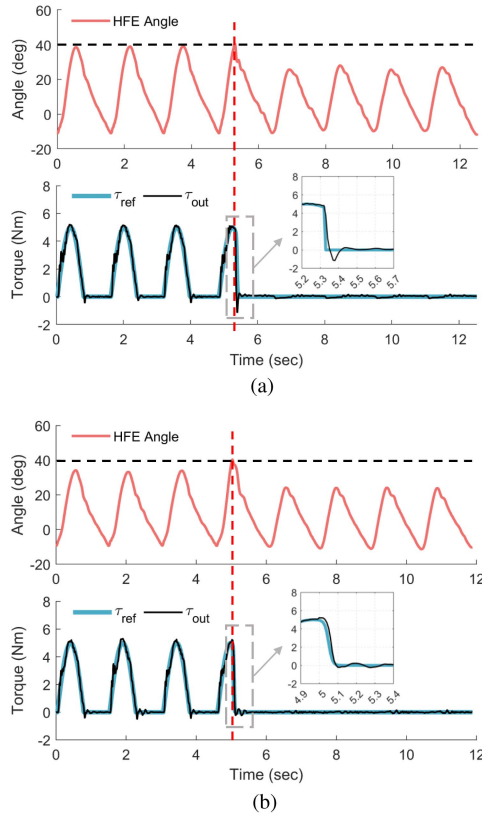


Fig. 9. Safety behaviors of the hip exoskeleton. (a) When the angle of hip flexion/extension exceeded the safety threshold, the exoskeleton was directly switched OFF. (b) When the angle of hip flexion/extension exceeded the safety threshold, the exoskeleton immediately switched from assistive mode to transparent mode with the control of the modified cascade PI controller.

C. Preliminary Safety Experiment

This experiment was performed to check if the hip exoskeleton driven by the nSEA can guarantee the user's safety when some unsafe behaviors happen during assistive walking. As can be seen from the experimental results shown in Fig. 9(a) and (b), with walking assistance from the hip exoskeleton, the angle of hip flexion is significantly increased. In order to protect the users from injuries, a safety threshold is necessary. When the angle of hip flexion/extension of the users exceeds the predetermined safety threshold, safety behaviors of the hip exoskeleton will be triggered. The value of the safety threshold in the article was only set for testing purposes, and the real value should be determined by the therapists based on the patients' condition in practical applications.

Fig. 9(a) shows one of the safety behaviors of the hip exoskeleton. When the angle of hip flexion/extension exceeded the safety threshold, the exoskeleton was directly switched OFF, which is more reliable and faster than any software-based or clutch-based safety behavior. Benefiting from low mechanical impedance and high backdrivability of the nSEA, the rms error of the interaction torque was only 0.067 N · m during the free walking period. Specifically, the timing of reaching a peak hip extension angle for the first time after the safety behavior was triggered was regarded as the start of the free walking period. Fig. 9(b) shows another safety behavior of the hip exoskeleton. When the angle of hip flexion/extension exceeded the safety threshold, the exoskeleton immediately switched from assistive mode to transparent mode with the control of the modified cascade PI controller. In order to achieve a smooth switch and reduce negative effects on the patients who are sensitive to external disturbances, the reference torque profile during the switching period is defined as the following equations and the duration of the switching period is controlled by the switching time Δt_{swi} :

$$h(t, \Delta t_{swi}) = \frac{1}{2} \tanh \left[\mu \left(\frac{1}{\Delta t_{swi}} t - \frac{1}{2} \right) \right] \quad (16)$$

$$\tau_{ref}(t) = \tau_0 h(t, \Delta t_{swi}) \quad (17)$$

where μ is a positive constant and τ_0 is the assistive torque applied to the subject's hip joint when the safety behavior is triggered.

Compared to the experimental results shown in Fig. 9(a), with the switching control of the modified cascade PI controller, the interaction torque and the angle of hip flexion/extension of the subject changed more smoothly, which is more friendly and safer for the patients who are sensitive to external disturbances because of muscle weakness and paralysis. During the free walking period, the rms error of the interaction torque was only 0.034 N · m with the zero-impedance control of the modified cascade PI controller.

V. DISCUSSION

Wearable robotic systems that physically interact with humans should guarantee safety, as well as stability and control performance. Mechanical impedance is an effective means to evaluate the safety of such systems and in general, systems with low mechanical impedance are regarded as safe systems in mechatronics [11]. The actual mechanical impedance of the nSEA is quantified by measuring resistance torque during motions, which is consistent with existing studies [6], [9], [18],

[32], [37]. Specifically, the resistance torque under the powered OFF and the zero-impedance condition represents the intrinsic mechanical impedance and the residual mechanical impedance after controller compensation, respectively.

As shown in Fig. 7(a), the rms resistance torque was only $0.143 \text{ N} \cdot \text{m}$ [0.72% of peak torque (PT)] during continuous walking when the exoskeleton was powered OFF, which represented the intrinsic mechanical impedance of the nSEA. By comparison, the ball screw-driven SEA presented in [9] exerted an rms resistance torque of $4.66 \text{ N} \cdot \text{m}$ (7.76% of PT) to the user's hip joint when the exoskeleton was powered OFF. In [9], the high mechanical impedance of exoskeleton joints and large undesired resistance torque also led to significant negative effects on the joint movement and energy expenditure of human users during walking, including limited walking speed (0.4 m/s), reduced hip joint's range of motion (reduced by more than 10 deg), and increased energy cost of walking (increased by 0.59 W/kg). In contrast, benefiting from the low mechanical impedance and high backdrivability of the nSEA, no significant reduction in the hip joint's range of motion and walking speed was found even the exoskeleton was powered OFF when compared to the without exoskeleton condition, and the metabolic cost during walking only increased by 0.08 W/kg compared to the with exoskeleton weight condition [see Figs. 7(b) and 8].

Direct comparison with existing nonlinear SEAs [19], [20], [21], [22] could not be performed because the rms resistance torque during walking conditions is rarely reported in the literature. Recently, some low-impedance actuators have been developed for highly backdrivable lower-limb exoskeletons, but these actuators still required $\sim 0.4 \text{ N} \cdot \text{m}$ (0.95% of PT) [37], $\sim 2 \text{ N} \cdot \text{m}$ (8.4% of PT) [32] to be backdriven, and the low mechanical impedance and high backdrivability were mainly achieved by adopting a low-ratio transmission. In our work, by combining a low-ratio transmission (6:1) and the optimized nonlinear stiffness profile ($6.7\text{--}112.9 \text{ N} \cdot \text{m/rad}$) generated by the reconfigurable RSEE, the proposed nSEA minimized inertia and friction in the transmission mechanism compared to existing SEAs, and low mechanical impedance, high force control fidelity, enough torque output, and bandwidth were yielded simultaneously. Moreover, the unique advantages of the nSEA (low mechanical impedance, high backdrivability, and compliance) also ensured the human users' safety during walking, which was verified by human subject tests, as shown in Fig. 9.

With effective impedance compensation from the modified cascade PI controller during walking, the rms resistance torque between the exoskeleton and the human user was further reduced from $0.143 \text{ N} \cdot \text{m}$ to $0.051 \text{ N} \cdot \text{m}$ (0.26% of PT), which demonstrated the excellent actuation transparency of the nSEA and also showed distinct advantage compared to existing SEAs applied in lower-limb exoskeletons [9], [18]. Compared to the hip exoskeleton driven by SEAs with high linear stiffness ($800 \text{ N} \cdot \text{m/rad}$) [18], in zero-impedance mode, the peak residual torque of our device was only $0.179 \text{ N} \cdot \text{m}$ (0.87% of PT), which was reported as no more than $1.4 \text{ N} \cdot \text{m}$ (1.75% of PT) at the same walking speed (1 m/s) in the cited reference. Furthermore, by using the zero-impedance controller, the rms resistance torque was significantly reduced from 4.66 to $0.94 \text{ N} \cdot \text{m}$ (1.56% of PT)

in [9]. But the residual torque was still large, and thus obvious reduction in peak hip flexion angle and increase in energy cost of walking can be observed. In our work, as shown in Figs. 7 and 8, the high actuation transparency minimized the negative influence of the undesired resistance torque on the hip joint's range of motion (without exo versus zero impedance: $40.03 \pm 0.63 \text{ deg}$ versus $43.00 \pm 1.17 \text{ deg}$) and energy cost (without exo versus with exo weight: $2.16 \pm 0.20 \text{ W/kg}$ versus $2.15 \pm 0.20 \text{ W/kg}$) during walking, which was negligible in practical applications.

Finally, beyond the advantages discussed above, the low mechanical impedance from reduced friction and gear meshings and the high compliance from the RSEE also lead to a quieter device, which is significant for the clinical acceptance of wearable exoskeleton devices.

VI. CONCLUSION AND FUTURE WORKS

In this work, we aim to develop a hip exoskeleton to provide walking assistance for incomplete paraplegic patients or elderly people with age-related mobility decline. A necessary requirement for the exoskeleton joints designed to assist or augment human motion is to have low mechanical impedance (that is, be highly backdrivable or transparent). In order to improve actuation transparency and safety of the hip exoskeleton, a novel nSEA is proposed, which weighs only 0.85 kg with a peak torque output of $19.8 \text{ N} \cdot \text{m}$. The nSEA-driven hip exoskeleton outperforms state-of-the-art works [9], [18], [32], [37] in terms of actuation transparency and pHRI safety while the desired assistive torque can be generated precisely with the proposed torque control when assistance is required. The control performance and stability have been analyzed and validated by experiments with human subjects.

Low mechanical impedance is a common requirement for pHRI [11]; thus, the proposed nSEA is also promising to be applied in other robots necessarily interacting with human, such as upper-limb rehabilitation robots or service robots. One possible limitation of the nSEA for wider applications is its relatively narrow torque bandwidth. Although the torque bandwidth of the nSEA is sufficient for the targeted application in this study, future work will specially develop a torque controller to further improve its torque bandwidth. Furthermore, for a specific application that requires larger torque bandwidth, we can also increase the torque bandwidth by choosing an RSEE configuration with a less nonlinear stiffness profile based on the reconfigurable design of the RSEE or replace the current springs by the ones with higher stiffness.

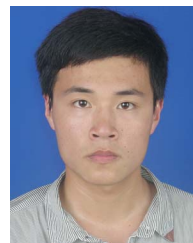
REFERENCES

- [1] H. Woo, B. Na, and K. Kong, "Design of a compact rotary series elastic actuator for improved actuation transparency and mechanical safety," in *Proc. IEEE Int. Conf. Robot. Automat.*, 2017, pp. 1872–1877.
- [2] T. Zhang and H. Huang, "Design and control of a series elastic actuator with clutch for hip exoskeleton for precise assistive magnitude and timing control and improved mechanical safety," *IEEE/ASME Trans. Mechatronics*, vol. 24, no. 5, pp. 2215–2226, Oct. 2019.
- [3] G. Aguirre-Ollinger and H. Yu, "Lower-limb exoskeleton with variable-structure series elastic actuators: Phase-synchronized force control for gait asymmetry correction," *IEEE Trans. Robot.*, vol. 37, no. 3, pp. 763–779, Jun. 2021.

- [4] Y. Qian et al., "Predictive locomotion mode recognition and accurate gait phase estimation for hip exoskeleton on various terrains," *IEEE Robot. Automat. Lett.*, vol. 7, no. 3, pp. 6439–6446, Jul. 2022.
- [5] G. Lv, H. Zhu, and R. D. Gregg, "On the design and control of highly backdrivable lower-limb exoskeletons: A discussion of past and ongoing work," *IEEE Control Syst. Mag.*, vol. 38, no. 6, pp. 88–113, Dec. 2018.
- [6] D. A. Lawrence, L. Y. Pao, M. A. Salada, and A. M. Dougherty, "Quantitative experimental analysis of transparency and stability in haptic interfaces," in *Proc. 5th Annu. Symp. Haptic Interfaces Virtual Environ. Teleoperator Syst.*, 1996, pp. 441–449.
- [7] G. Aguirre-Ollinger, J. E. Colgate, M. A. Peshkin, and A. Goswami, "Inertia compensation control of a one-degree-of-freedom exoskeleton for lower-limb assistance: Initial experiments," *IEEE Trans. Neural Syst. Rehabil. Eng.*, vol. 20, no. 1, pp. 68–77, Jan. 2012.
- [8] D. Zanotto, T. Lenzi, P. Stegall, and S. K. Agrawal, "Improving transparency of powered exoskeletons using force/torque sensors on the supporting cuffs," in *Proc. IEEE 13th Int. Conf. Rehabil. Robot.*, 2013, pp. 1–6.
- [9] I. Kang, H. Hsu, and A. Young, "The effect of hip assistance levels on human energetic cost using robotic hip exoskeletons," *IEEE Robot. Automat. Lett.*, vol. 4, no. 2, pp. 430–437, Apr. 2019.
- [10] K. Kong, H. Moon, B. Hwang, D. Jeon, and M. Tomizuka, "Impedance compensation of SUBAR for back-drivable force-mode actuation," *IEEE Trans. Robot.*, vol. 25, no. 3, pp. 512–521, Jun. 2009.
- [11] H. Woo and K. Kong, "Controller design for mechanical impedance reduction," *IEEE/ASME Trans. Mechatronics*, vol. 20, no. 2, pp. 845–854, Apr. 2015.
- [12] S. Oh, H. Woo, and K. Kong, "Frequency-shaped impedance control for safe human–robot interaction in reference tracking application," *IEEE/ASME Trans. Mechatronics*, vol. 19, no. 6, pp. 1907–1916, Dec. 2014.
- [13] G. A. Pratt and M. M. Williamson, "Series elastic actuators," in *Proc. IEEE/RSJ Int. Conf. Intell. Robots Syst.*, 1995, pp. 399–406.
- [14] K. Kong, J. Bae, and M. Tomizuka, "Control of rotary series elastic actuator for ideal force-mode actuation in human–robot interaction applications," *IEEE/ASME Trans. Mechatronics*, vol. 14, no. 1, pp. 105–118, Feb. 2009.
- [15] T. Chen, R. Casas, and P. S. Lum, "An elbow exoskeleton for upper limb rehabilitation with series elastic actuator and cable-driven differential," *IEEE Trans. Robot.*, vol. 35, no. 6, pp. 1464–1474, Dec. 2019.
- [16] D. W. Robinson, "Design and analysis of series elasticity in closed-loop actuator force control," Ph.D. dissertation, Dept. Mech. Eng., Massachusetts Inst. Technol., Cambridge, MA, USA, 2000.
- [17] S. Wang et al., "Design and control of the MINDWALKER exoskeleton," *IEEE Trans. Neural Syst. Rehabil. Eng.*, vol. 23, no. 2, pp. 277–286, Mar. 2015.
- [18] T. Zhang, M. Tran, and H. Huang, "Admittance shaping-based assistive control of SEA-driven robotic hip exoskeleton," *IEEE/ASME Trans. Mechatronics*, vol. 24, no. 4, pp. 1508–1519, Aug. 2019.
- [19] B. Vanderborght, N. G. Tsagarakis, C. Semini, R. Van Ham, and D. G. Caldwell, "MACCEPA 2.0: Adjustable compliant actuator with stiffening characteristic for energy efficient hopping," in *Proc. IEEE Int. Conf. Robot. Automat.*, 2009, pp. 544–549.
- [20] I. Thorson and D. Caldwell, "A nonlinear series elastic actuator for highly dynamic motions," in *Proc. IEEE/RSJ Int. Conf. Intell. Robots Syst.*, 2011, pp. 390–394.
- [21] J. Austin, A. Schepelmann, and H. Geyer, "Control and evaluation of series elastic actuators with nonlinear rubber springs," in *Proc. IEEE/RSJ Int. Conf. Intell. Robots Syst.*, 2015, pp. 6563–6568.
- [22] L. Zhou, W. Chen, W. Chen, S. Bai, J. Wang, and J. Zhang, "Design of a compact rotary series elastic actuator with nonlinear stiffness for lower limb exoskeletons," in *Proc. IEEE/ASME Int. Conf. Adv. Intell. Mechatronics*, 2019, pp. 68–73.
- [23] J. Sun, Z. Guo, Y. Zhang, X. Xiao, and J. Tan, "A novel design of serial variable stiffness actuator based on an Archimedean spiral relocation mechanism," *IEEE/ASME Trans. Mechatronics*, vol. 23, no. 5, pp. 2121–2131, Oct. 2018.
- [24] Y. Zhu, Q. Wu, B. Chen, D. Xu, and Z. Shao, "Design and evaluation of a novel torque-controllable variable stiffness actuator with reconfigurability," *IEEE/ASME Trans. Mechatronics*, vol. 27, no. 1, pp. 292–303, Feb. 2022.
- [25] Y. Qian, S. Han, G. Aguirre-Ollinger, C. Fu, and H. Yu, "Design, modeling, and control of a reconfigurable rotary series elastic actuator with nonlinear stiffness for assistive robots," *Mechatronics*, vol. 86, 2022, Art. no. 102872.
- [26] H. Vallery et al., "Compliant actuation of rehabilitation robots," *IEEE Robot. Automat. Mag.*, vol. 15, no. 3, pp. 60–69, Sep. 2008.
- [27] J. W. Sensinger and R. F. F. Weir, "Improvements to series elastic actuators," in *Proc. 2nd IEEE/ASME Int. Conf. Mechatronics Embedded Syst. Appl.*, 2006, pp. 1–7.
- [28] F. E. Tosun and V. Patoglu, "Necessary and sufficient conditions for the passivity of impedance rendering with velocity-sourced series elastic actuation," *IEEE Trans. Robot.*, vol. 36, no. 3, pp. 757–772, Jun. 2020.
- [29] L. Sun, M. Li, M. Wang, W. Yin, N. Sun, and J. Liu, "Continuous finite-time output torque control approach for series elastic actuator," *Mech. Syst. Signal Process.*, vol. 139, 2020, Art. no. 105853.
- [30] M. Grimmer and A. Seyfarth, "Mimicking human-like leg function in prosthetic limbs," in *Neuro-Robotics*. Berlin, Germany: Springer, 2014, pp. 105–155.
- [31] D. A. Winter, *Biomechanics and Motor Control of Human Movement*. Hoboken, NJ, USA: Wiley, 2009.
- [32] H. Zhu, C. Nesler, N. Divekar, V. Peddinti, and R. D. Gregg, "Design principles for compact, backdrivable actuation in partial-assist powered knee orthoses," *IEEE/ASME Trans. Mechatronics*, vol. 26, no. 6, pp. 3104–3115, Dec. 2021.
- [33] M. Keppler, D. Lakatos, C. Ott, and A. Albu-Schäffer, "Elastic structure preserving (ESP) control for compliantly actuated robots," *IEEE Trans. Robot.*, vol. 34, no. 2, pp. 317–335, Apr. 2018.
- [34] H. Yu, S. Huang, G. Chen, Y. Pan, and Z. Guo, "Human–robot interaction control of rehabilitation robots with series elastic actuators," *IEEE Trans. Robot.*, vol. 31, no. 5, pp. 1089–1100, Oct. 2015.
- [35] J. Brockway, "Derivation of formulae used to calculate energy expenditure in man," *Hum. Nutr. Clin. Nutr.*, vol. 41, no. 6, pp. 463–471, 1987.
- [36] T. M. Griffin, T. J. Roberts, and R. Kram, "Metabolic cost of generating muscular force in human walking: Insights from load-carrying and speed experiments," *J. Appl. Physiol.*, vol. 95, no. 1, pp. 172–183, 2003.
- [37] S. Yu et al., "Quasi-direct drive actuation for a lightweight hip exoskeleton with high backdrivability and high bandwidth," *IEEE/ASME Trans. Mechatronics*, vol. 25, no. 4, pp. 1794–1802, Aug. 2020.



Yuepeng Qian (Graduate Student Member, IEEE) received the B.E. degree in mechanical engineering from Tsinghua University, Beijing, China, in 2018. He is currently working toward the Ph.D. degree in biomedical engineering with the National University of Singapore, Singapore. His research interests include compliant actuator, physical human–robot interaction, lower-limb exoskeleton, and assistive strategies.



Shuaishuai Han (Member, IEEE) received the B.E. degree in automation and the Ph.D. degree in control science and engineering from Nanjing University of Science and Technology, Nanjing, China, in 2015 and 2021, respectively. He is currently a Research Fellow with the National University of Singapore, Singapore. His research interests include the design of rehabilitation strategies, wearable exoskeleton, and robot control.



Yining Wang received the B.E. degree in mechanical design & manufacturing and their automation from Southwest University of Science and Technology, Mianyang, China, in 2019, and the M.S. degree in mechanics from Southern University of Science and Technology, Shenzhen, China, in 2022. Her research interests include gait analysis and exoskeleton control for hemiplegic patients.



Haoyong Yu (Senior Member, IEEE) received the B.S. and M.S. degrees from Shanghai Jiao Tong University, Shanghai, China, in 1988 and 1991, respectively, and the Ph.D. degree from the Massachusetts Institute of Technology, Cambridge, MA, USA, in 2002, all in mechanical engineering.

He is currently an Associate Professor with the Department of Biomedical Engineering, National University of Singapore, Singapore. His research interests include medical robotics, rehabilitation engineering and assistive technologies, system dynamics, and control.



Chenglong Fu (Member, IEEE) received the B.S. degree from Tongji University, Shanghai, China, in 2002, and the Ph.D. degree from Tsinghua University, Beijing, China, in 2007, all in mechanical engineering.

He was an Associate Professor with Tsinghua University and a Visiting Scholar with the University of Michigan at Ann Arbor, Ann Arbor, MI, USA. He is currently a Professor with the Department of Mechanical and Energy Engineering, Southern University of Science and Technology, Shenzhen, China. His research interests include wearable robots and human-centered robotics.